npj computational materials

www.nature.com/npjcompumats

ARTICLE OPEN

Substrate effects on spin relaxation in two-dimensional Dirac materials with strong spin-orbit coupling

Junqing Xu[1]✉ and Yuan Ping[1]✉

Understanding substrate effects on spin dynamics and relaxation is of key importance for spin-based information technologies. However, the key factors that determine such effects, in particular for materials with strong spin-orbit coupling (SOC), have not been well understood. Here we performed first-principles real-time density-matrix dynamics simulations with SOC and the electron-phonon and electron-impurity scattering for spin lifetimes (τ_s) of supported/free-standing germanene, a prototypical strong SOC 2D Dirac material. We show that the effects of different substrates on τ_s can surprisingly differ by two orders of magnitude. We find that substrate effects on τ_s are closely related to substrate-induced modifications of the SOC-field anisotropy, which changes the spin-flip scattering matrix elements. We propose a new electronic quantity, named spin-flip angle $\theta^{\uparrow\downarrow}$, to characterize spin relaxation through intervalley spin-flip scattering. We find that τ_s^{-1} is approximately proportional to the averaged value of $\sin^2\left(\theta^{\uparrow\downarrow}/2\right)$, which serves as a guiding parameter of controlling spin relaxation.

npj Computational Materials (2023)9:47 ; https://doi.org/10.1038/s41524-023-00992-y

INTRODUCTION

Since the long spin diffusion length (l_s) in large-area graphene was first reported by Tombros et al.[1], significant advances have been made in the field of spintronics, which has the potential to realize low-power electronics by utilizing spin as the information carrier. Various 2D materials have shown promising spintronic properties[2], e.g., long l_s at room temperatures in graphene[3] and ultrathin black phosphorus[4], spin-valley locking (SVL) and ultralong spin lifetime τ_s at low temperatures in transition metal dichalcogenides (TMDs)[5] and germanene[6], and persistent spin helix in 2D hybrid perovskites[7], which satisfies SU(2) symmetry and potentially could enhance spin lifetime significantly[8].

Understanding spin relaxation and transport mechanism in materials is of key importance for spintronics and spin-based quantum information technologies. One critical metric for ideal materials in such applications is spin lifetime (τ_s), often required to be sufficiently long for stable detection and manipulation of spin. In 2D-material-based spintronic devices, the materials are usually supported on a substrate. Therefore, for the design of those devices, it is crucial to understand substrate effects on spin relaxation. In past work, the substrate effects were mostly studied for weak SOC Dirac materials like graphene[9–13]. How substrates affect strong SOC Dirac materials like germanene is unknown. In particular, the spin relaxation mechanism between weak and strong SOC Dirac materials was shown to be drastically different[6]. Therefore, careful investigations are required to unveil the distinct substrate effects on these two types of materials.

Here we focus on the dangling-bond-free insulating substrates, which interact weakly with the material thus preserve its main physical properties. Insulating substrates can affect spin dynamics and relaxation in several aspects: (i) They may induce strong SOC fields, so called internal magnetic fields $\mathbf{B}^{\text{in}}$ (which determine spin textures or helices) by breaking inversion symmetry[10] or through proximity effects[11]. For example, the hexagonal boron nitride substrate can induce Rashba-like fields on graphene and dramatically accelerate its spin relaxation and enhance the anisotropy of τ_s between in-plane and out-of-plane directions[9]. (ii) Substrates may introduce additional impurities[12,13] or reduce impurities/defects in material layers, e.g., by encapsulation[14]. In consequence, substrates may change the electron-impurity (e-i) scattering strength, which affects spin relaxation through SOC. (iii) Thermal vibrations of substrate atoms can introduce additional spin-phonon scattering by interacting with spins of materials[10].

Previously most theoretical studies of substrate effects on spin relaxation were done based on model Hamiltonian and simplified spin relaxation models[10,12,13]. While those models provide rich mechanistic insights, they are lack of predictive power and quantitative accuracy, compared to first-principles theory. On the other hand, most first-principles studies only simulated the band structures and spin polarizations/textures of the heterostructures[15–17], which are not adequate for understanding spin relaxation. Recently, with our newly-developed first-principles density-matrix (FPDM) dynamics approach, we studied the hBN substrate effect on spin relaxation of graphene, a weak SOC Dirac material. We found a dominant D'yakonov-Perel' (DP) mechanism and nontrivial modification of SOC fields and electron-phonon coupling by substrates[9]. However, strong SOC Dirac materials can have a different spin relaxation mechanism - Elliott-Yafet (EY) mechanism[18], with only spin-flip transition and no spin precession, unlike the DP mechanism. How substrates affect spin relaxation of materials dominated by EY mechanism is the key question here. Furthermore, how such effects vary among different substrates is another outstanding question for guiding experimental design of interfaces.

In our recent study, we have predicted that monolayer germanene (ML-Ge) is a promising material for spin-valleytronic applications, due to its excellent properties including spin-valley locking, long τ_s and l_s, and highly tunable spin properties by varying gates and external fields[6]. As discussed in ref. [6], ML-Ge has strong intrinsic SOC unlike graphene and silicene. Under an out-of-plane electric field (in consequence broken inversion symmetry), a strong out-of-plane internal magnetic field forms, which may lead to mostly EY spin relaxation[6]. Therefore, predicting τ_s of supported ML-Ge is important for future applications and our

[1]Department of Chemistry and Biochemistry, University of California, Santa Cruz, CA 95064, USA. ✉email: jxu153@ucsc.edu; yuanping@ucsc.edu

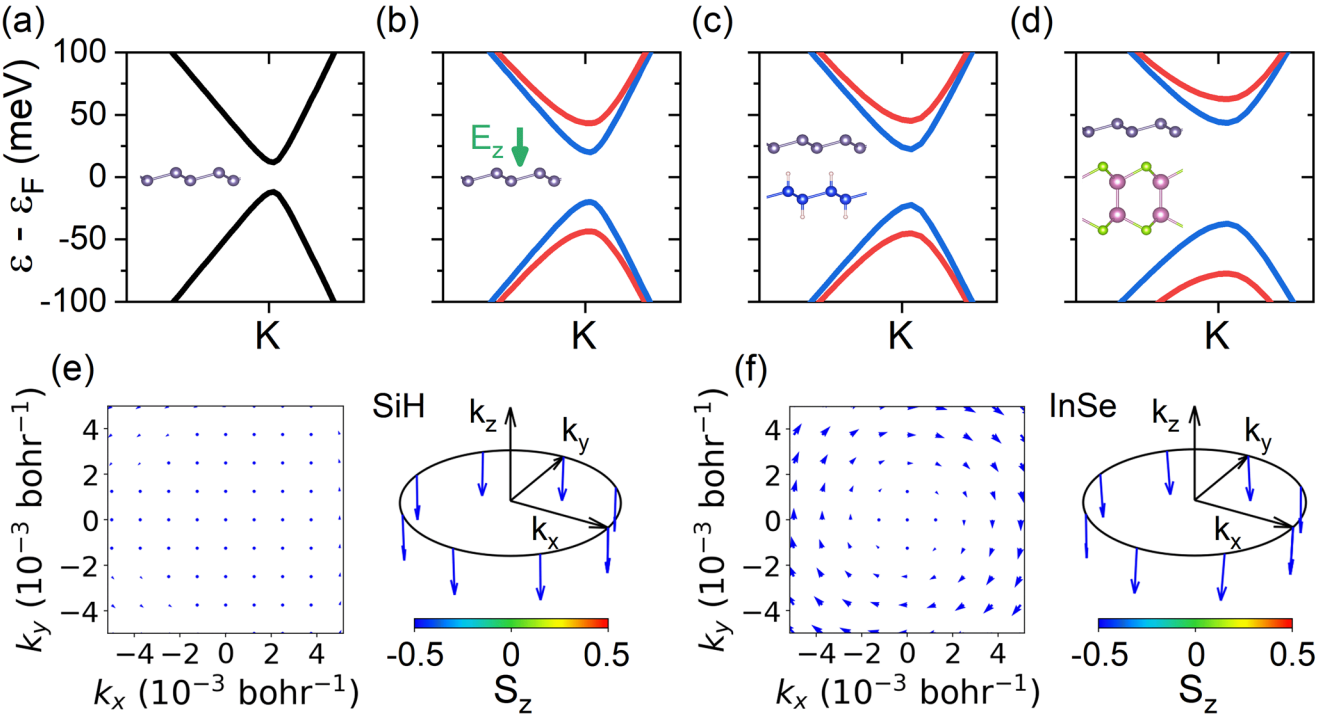

Fig. 1 Band structures and spin textures around the Dirac cones of ML-Ge systems with and without substrates. Band structures of ML-Ge under $E_z = 0$ **a** and under -7 V/nm **b**, ML-Ge on silicane (SiH) **c**, and on InSe substrates **d** are shown, respectively. The red and blue bands correspond to spin-up and spin-down states. Due to time-reversal symmetry, band structures around another Dirac cone at $K' = -K$ are the same except that the spin-up and spin-down bands are reversed. The gray, white, blue, pink, and green balls correspond to Ge, H, Si, In, and Se atoms, respectively. Band structures of ML-Ge on germanane (GeH) and GaTe are shown in Supplementary Fig. 4 in the Supporting Information, and are similar to those of ML-Ge on SiH and InSe substrates, respectively. Spin textures in the k_x–k_y plane (**e** and **f**, left) and 3D plots of the spin vectors $\mathbf{S}^{\rm exp}_{k_1}$ on the circle $|\vec{k}| = 0.005$ bohr^{-1} of the band edge around K of ML-Ge on SiH (**e**, right) and InSe substrates (**f**, right) are shown. $\mathbf{S}^{\rm exp} \equiv (S^{\rm exp}_x, S^{\rm exp}_y, S^{\rm exp}_z)$ with $S^{\rm exp}_i$ being spin expectation value along direction i and is the diagonal element of spin matrix s_i in Bloch basis. The color scales $S^{\rm exp}_z$ and the arrow length scales the vector length of the in-plane spin expectation value.

understanding of substrate effects on strong SOC materials. Here, we examine the substrate effects on spin relaxation in ML-Ge through FPDM simulations, with self-consistent SOC and quantum descriptions of e-ph and e-i scattering processes[6,9,19–21]. We study free-standing ML-Ge and ML-Ge supported by four different insulating substrates - germanane (GeH), silicane (SiH), GaTe and InSe. The choice of substrates is based on similar lattice constants to ML-Ge, preservation of Dirac Cones, and experimental synthesis accessibility[22,23]. We will first show how electronic structures and τ_s of ML-Ge are changed by different substrates - while τ_s of ML-Ge on GeH and SiH are similar to free-standing ML-Ge, the GaTe and InSe substrates strongly reduce τ_s of ML-Ge due to stronger interlayer interactions. We then discuss what quantities are responsible for the disparate substrate effects on spin relaxation, which eventually answered the outstanding questions we raised earlier.

RESULTS

Substrate effects on electronic structure and spin texture

We begin with comparing band structures and spin textures of free-standing and supported ML-Ge in Fig. 1, which are essential for understanding spin relaxation mechanisms. Since one of the most important effects of a substrate is to induce an out-of-plane electric field E_z on the material layer, we also study ML-Ge under a constant E_z as a reference. The choice of the E_z is based on reproducing a similar band splitting to the one in ML-Ge with substrates. The band structure of ML-Ge is similar to graphene with two Dirac cones at K and $K' \equiv -K$, but a larger band gap of 23 meV. At $E_z = 0$, due to time-reversal and inversion symmetries of ML-Ge, every two bands form a Kramers degenerate pair[18]. A finite E_z or a substrate breaks the inversion symmetry and induces a strong out-of-plane internal B field $\mathbf{B}^{\rm in}$ (Eq. (21)), which splits the Kramers pairs into spin-up and spin-down bands[6]. Interestingly, we find that band structures of ML-Ge-SiH (Fig. 1c) and ML-Ge-GeH (Supplementary Fig. 4) are quite similar to free-standing ML-Ge under $E_z = -7$ V/nm (ML-Ge@-7 V/nm, Fig. 1b), which indicates that the impact of the SiH/GeH substrate on band structure and $\mathbf{B}^{\rm in}$ may be similar to a finite E_z (Supplementary Fig. 4). This similarity is frequently assumed in model Hamiltonian studies[10,12]. On the other hand, the band structures of ML-Ge-InSe (Fig. 1d) and ML-Ge-GaTe (Supplementary Fig. 4) have more differences from the free-standing one under E_z, with larger band gaps, smaller band curvatures at Dirac Cones, and larger electron-hole asymmetry of band splittings. This implies that the impact of the InSe/GaTe substrates can not be approximated by applying an E_z to the free-standing ML-Ge, unlike SiH/GeH substrates.

We further examine the spin expectation value vectors $\mathbf{S}^{\rm exp}$ of substrate-supported ML-Ge. $\mathbf{S}^{\rm exp}$ is parallel to $\mathbf{B}^{\rm in}$ by definition (Eq. (21)). $\mathbf{S}^{\rm exp} \equiv (S^{\rm exp}_x, S^{\rm exp}_y, S^{\rm exp}_z)$ with $S^{\rm exp}_i$ being spin expectation value along direction i and is the diagonal element of spin matrix s_i in Bloch basis. Importantly, from Fig. 1e, f, although $\mathbf{S}^{\rm exp}$ of ML-Ge on substrates are highly polarized along z (out-of-plane) direction, the in-plane components of $\mathbf{S}^{\rm exp}$ of ML-Ge-InSe (and ML-Ge-GaTe) are much more pronounced than ML-Ge-SiH (and ML-Ge-GeH). Such differences are crucial to the out-of-plane spin relaxation as discussed in a later subsection.

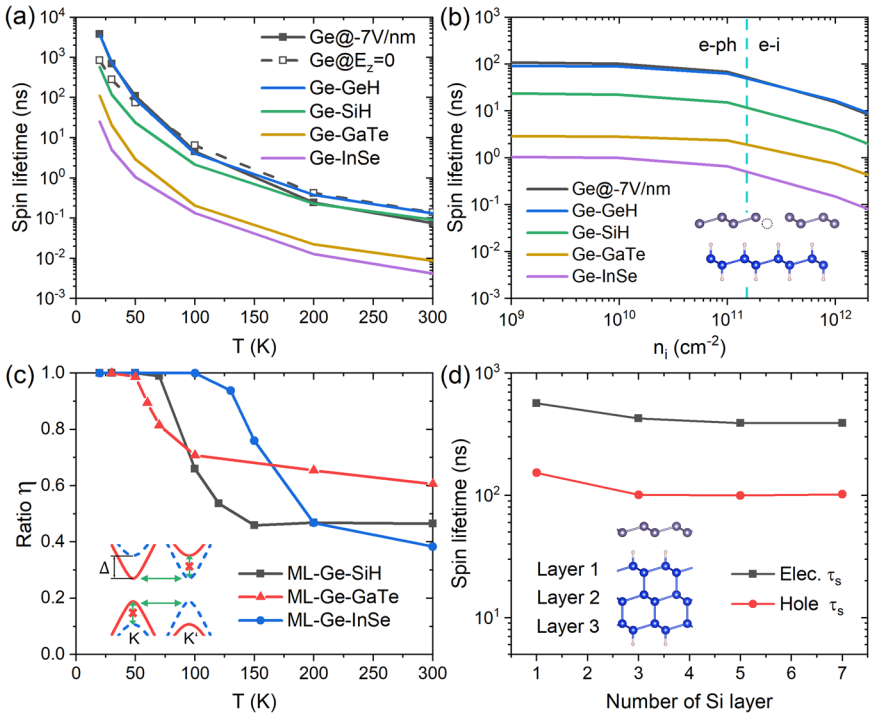

Fig. 2 The out-of-plane spin lifetime τ_s of intrinsic free-standing and substrate-supported ML-Ge. a τ_s of ML-Ge under $E_z = 0$, -7 V/nm and substrate-supported ML-Ge as a function of temperature without impurities. Here we show electron τ_s for intrinsic ML-Ge systems except that hole τ_s is shown for ML-Ge-InSe, since electron τ_s are longer than hole τ_s at low T except ML-Ge-InSe. **b** τ_s as a function of impurity density n_i at 50 K. The impurities are neutral ML-Ge vacancy with 50% at higher positions and 50% at lower ones of a Ge layer. The dashed vertical line corresponds to the impurity density where e-ph and e-i scatterings contribute equally to spin relaxation ($n_{i,s}$). And e-ph (e-i) scattering is more dominant if $n_i < (>) n_{i,s}$. **c** The proportion of intervalley spin relaxation contribution η of (electrons of) ML-Ge-SiH and (holes of) ML-Ge-InSe without impurities. η is defined as $\eta = \frac{\left(\tau_{s,z}^{\text{inter}}\right)^{-1}}{\left(\tau_{s,z}^{\text{inter}}\right)^{-1} + w\left(\tau_{s,z}^{\text{intra}}\right)^{-1}}$, where $\tau_{s,z}^{\text{inter}}$ and $\tau_{s,z}^{\text{intra}}$ are intervalley and intravalley spin lifetimes, corresponding to scattering processes between K and K' valleys and within a single K or K' valley, respectively. η being close to 1 or 0 corresponds to dominant intervalley or intravalley spin relaxation, respectively. w is a weight factor related to what percentage of total S_z can be relaxed out by intravalley scattering itself. w being close to 0 and 1 correspond to the cases that intravalley scattering can only relax a small part (0) and most of excess spin (1) respectively. In Supplementary Note 2, we give more details about definition of w. **d** Electron and hole τ_s at 20 K of ML-Ge without impurities on hydrogen-terminated multilayer Si, labeled as Si_nH with n being number of Si layers. Si_nH is silicane if $n = 1$, and hydrogen-terminated Silicon (111) surface if $n = \infty$.

Spin lifetimes of germanene on substrates and spin relaxation mechanism

We then perform our first-principles density-matrix calculation[6,19–21] at proposed interfaces, and examine the role of electron-phonon coupling in spin relaxation of ML-Ge at different substrates. Throughout this paper, we focus on out-of-plane τ_s of ML-Ge systems, since their in-plane τ_s is too short and less interesting. We compare out-of-plane τ_s due to e-ph scattering between the free-standing ML-Ge (with/without an electric field) and ML-Ge on different substrates in Fig. 2a. Here we show electron τ_s for most ML-Ge/substrate systems as intrinsic semiconductors, except hole τ_s for the ML-Ge-InSe interface. This choice is because electron τ_s are mostly longer than hole τ_s at low T except for the one at the ML-Ge-InSe interface; longer lifetime is often more advantageous for spintronics applications. From Fig. 2, we find that τ_s of ML-Ge under $E_z = 0$ and -7 V/nm are at the same order of magnitude for a wide range of temperatures. The differences are only considerable at low T, e.g, by 3-4 times at 20 K. On the other hand, τ_s of supported ML-Ge are very sensitive to the specific substrates. While τ_s of ML-Ge-GeH and ML-Ge-SiH have the same order of magnitude as the free-standing ML-Ge, in particular very close between ML-Ge-GeH and ML-Ge@-7 V/nm, τ_s of ML-Ge-GaTe and ML-Ge-InSe are shorter by at least 1–2 orders of magnitude in the whole temperature range. This separates the substrates into two categories, i.e., with a weak effect (ML-Ge-GeH and ML-Ge-SiH) and a strong effect (ML-Ge-GaTe and ML-Ge-InSe).

We further investigate the role of electron-impurity (e-i) scattering in spin relaxation under different substrates, by introducing defects in the material layer. We consider a common type of impurity - single neutral Ge vacancy, whose formation energy was found relatively low in previous theoretical studies[24,25]. From Fig. 2b, we can see that τ_s of all five systems decrease with impurity density n_i. Since carrier scattering rates τ_p^{-1} (carrier lifetime τ_p) increases (decrease) with n_i, we then obtain τ_s decreases with τ_p's decrease, an evidence of EY spin relaxation mechanism. Moreover, we find that τ_s is sensitive to the type of the substrate with all values of n_i, and for each of four substrates, τ_s is reduced by a similar amount with different n_i, from low density limit (10^9 cm^{-2}, where e-ph scattering dominates) to relatively high density (10^{12} cm^{-2}, where e-i scattering becomes more important).

Since the bands near the Fermi energy are composed of the Dirac cone electrons around K and K' valleys in ML-Ge, spin relaxation process arises from intervalley and intravalley e-ph scatterings. We then examine relative intervalley spin relaxation contribution η (see its definition in the Fig. 2 caption) in Fig. 2c. η being close to 1 or 0 corresponds to intervalley or intravalley scattering being dominant in spin relaxation. η becomes close to 1 below 70 K for electrons of ML-Ge-SiH, and below 120 K for holes of ML-Ge-InSe. This indicates that at low T only intervalley scattering processes are relevant to spin relaxation in ML-Ge on substrates. This is a result of *spin-valley locking* (SVL), i.e., large

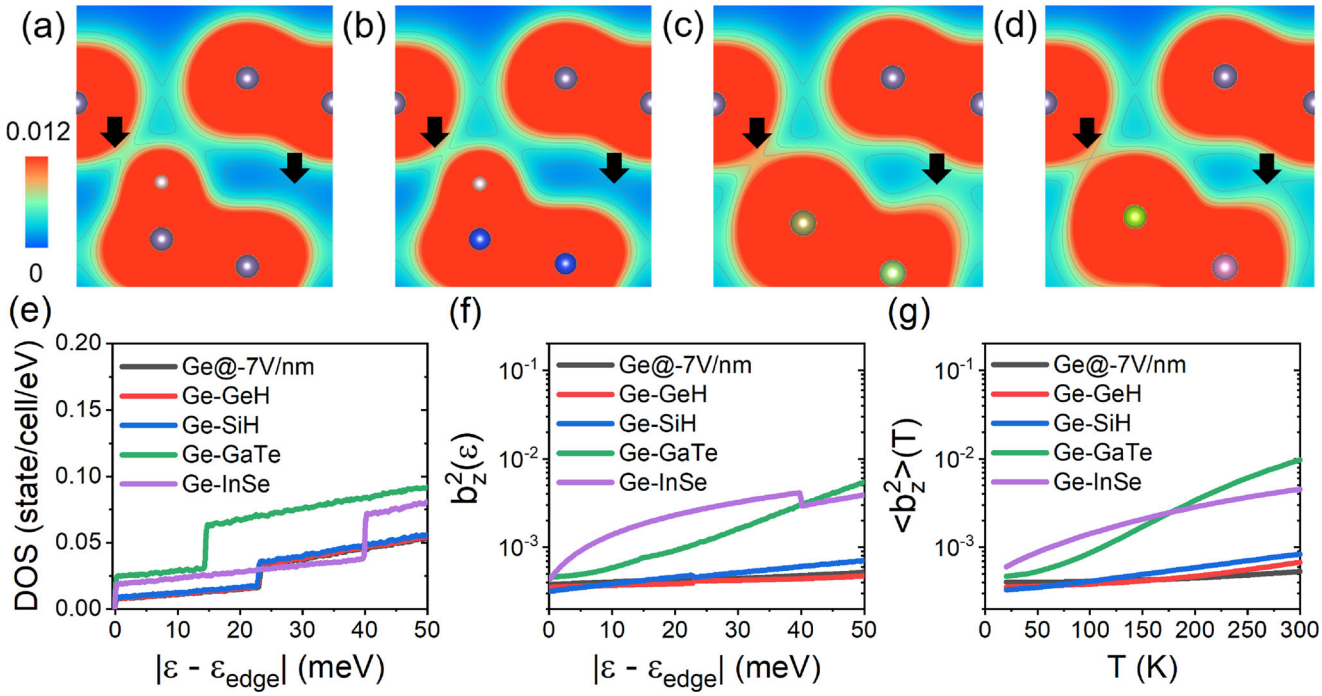

Fig. 3 Charge density, density of states (DOS), and spin-mixing parameters of free-standing and substrate-supported ML-Ge. Cross-section views of charge density at interfaces of ML-Ge on **a** GeH, **b** SiH, **c** GaTe, and **d** InSe. The Ge layers are above the substrate layers. The unit of charge density is e/bohr^3. Charge densities in the regions pointed out by black arrows show significant differences among different systems. **e** DOS and **f** energy-solved spin-mixing parameter along z axis $b_z^2(\varepsilon)$ of ML-Ge under $E_z = -7$ V/nm and on different substrates. ε_{edge} is the band edge energy at the valence band maximum or conduction band minimum. The step or sudden jump in the DOS curve corresponds to the edge energy of the second conduction/valence band or the SOC-induced splitting energy at K. **g** The temperature-dependent effective spin-mixing parameter $\langle b_z^2 \rangle$ of various ML-Ge systems.

SOC-induced band splittings lock up or down spin with a particular K or K′ valley[6]. According to Figs. 1 and 2c, the SVL transition temperature (T^{SVL}; below which the proportion of intervalley spin relaxation rate $\eta > 0.95$) seems approximately proportional to SOC splitting energy Δ^{SOC}, e.g., for electrons (CBM) of ML-Ge-GaTe and ML-Ge-SiH, and for holes (VBM) of ML-Ge-InSe, Δ^{SOC} are ~15, ~24 and 40 meV respectively, while T^{SVL} are 50, 70 and 120 K respectively. As Δ^{SOC} can be tuned by E_z and the substrate, T^{SVL} can be tuned simultaneously. Under SVL condition, spin or valley lifetime tends to be exceptionally long, which is ideal for spin-/valleytronic applications.

Additionally, the studied substrates here are monolayer, while practically multilayers or bulk are more common, thus it is necessary to understand how τ_s changes with the number of substrate layers. In Fig. 2d, we show τ_s at 20 K of ML-Ge on hydrogen-terminated multilayer Si, ML-Ge-Si$_n$H, with n being number of Si layer. Si$_n$H becomes hydrogen-terminated Silicon (111) surface if $n = \infty$. We find that τ_s are changed by only 30%-40% by increasing n from 1 to 3 and kept unchanged after $n \geq 3$. For generality of our conclusion, we also test the layer dependence of a different substrate. We found the τ_s of ML-Ge on bilayer InSe ($n = 2$) is changed by ~8% compared to monolayer InSe at 20 K, even smaller change than the one at Si$_n$H substrates. Given the disparate properties of these two substrates, we conclude using a monolayer is a reasonable choice for simulating the substrate effects on τ_s in this work.

The correlation of electronic structure and phonon properties to spin relaxation at different substrates

We next analyze in detail the relevant physical quantities, and determine the key factors responsible for substrate effects on spin relaxation. We focus on results under low T as spin relaxation properties are superior at lower T (the realization of SVL and longer τ_s).

First, to have a qualitative understanding of the material-substrate interaction strength, we show charge density distribution at the cross-section of interfaces in Fig. 3a–d. It seems that four substrates can be categorized into two groups: group A contains GeH and SiH with lower charge density distribution in the bonding regions (pointed by the arrows); group B contains GaTe and InSe with higher charge density distribution in the bonding regions. In Supplementary Fig. 5, we investigate the charge density change $\Delta\rho^e$ (defined by the charge density difference between interfaces and individual components). Consistent with Fig. 3, we find that $\Delta\rho^e$ for GaTe and InSe substrates overall has larger magnitude than the one for GeH and SiH substrates. Therefore the material-substrate interactions of group B seem stronger than those of group A. Intuitively, we may expect that the stronger the interaction, the stronger the substrate effect is. The FPDM simulations in Fig. 2a, b indeed show that the substrate effects of group B being stronger than those of group A on τ_s, consistent with the above intuition.

Next we examine electronic quantities closely related to spin-flip scattering responsible to EY spin relaxation. Qualitatively, for a state k_1, its spin-flip scattering-rate $\tau_s^{-1}(k_1)$ is proportional to the number of its pair states k_2 allowing spin-flip transitions between them. The number of pair states is approximately proportional to density of states (DOS) around the energy of k_1. Moreover, for EY mechanism, it is commonly assumed that spin relaxation rate is proportional to the degree of mixture of spin-up and spin-down states (along the z direction here), so called "spin-mixing" parameter[18] b_z^2 (see its definition in Supplementary Note 2), i.e., $\tau_s^{-1} \propto \langle b_z^2 \rangle$, where $\langle b_z^2 \rangle$ is the statistically averaged spin-mixing parameter as defined in ref. [6]. Therefore, we show DOS, energy-

Table 1. The phonon energy at wavevector K of the mode that contributes the most to spin relaxation, and the percentage of its contribution for various systems at 20 K.

Substrate	ω_K (meV)	Contribution
Ge@-7 V/nm	7.7	78%
Ge-GeH	6.9	70%
Ge-SiH	7.1	64%
Ge-GaTe	6.4	90%
Ge-InSe	7.2	99%

We consider momentum transfer K, as spin relaxation is fully determined by intervalley processes between K and K' valleys.

resolved spin-mixing $b_z^2(\varepsilon)$ and $\langle b_z^2 \rangle$ as a function of temperature in Fig. 3e–g.

We find that in Fig. 3e DOS of ML-Ge-GeH and ML-Ge-SiH are quite close to that of ML-Ge@-7 V/nm, while DOS of ML-Ge-GaTe and ML-Ge-InSe are 50%-100% higher around the band edge. Such DOS differences are qualitatively explained by the staggered potentials of ML-Ge-GaTe and ML-Ge-InSe being greater than those of ML-Ge-GeH and ML-Ge-SiH according to the model Hamiltonian proposed in ref. [26]. In Fig. 3f, g, b_z^2 of ML-Ge-GeH and ML-Ge-SiH are found similar to ML-Ge@-7 V/nm, and not sensitive to energy and temperature. On the contrast, for ML-Ge-GaTe and ML-Ge-InSe, their $b_z^2(\varepsilon)$ and $\langle b_z^2 \rangle$ increase rapidly with energy and temperature. Specifically, we can see at 300 K, $\langle b_z^2 \rangle$ of ML-Ge-GaTe and ML-Ge-InSe are about 4-20 times of the one of ML-Ge-GeH and ML-Ge-SiH in Fig. 3g. Thus the one order of magnitude difference of τ_s between group A (ML-Ge-GeH and ML-Ge-SiH) and group B (ML-Ge-GaTe and ML-Ge-InSe) substrates at 300 K can be largely explained by the substrate-induced changes of DOS and $\langle b_z^2 \rangle$. On the other hand, at low T, e.g., at 50 K, $\langle b_z^2 \rangle$ of ML-Ge-GaTe and ML-Ge-InSe are only about 1.5 and 2.5 times of the ones of ML-Ge-GeH and ML-Ge-SiH, and DOS are only tens of percent higher. However, there is still 1-2 order of magnitude difference of τ_s between different substrates. Therefore, the substrate effects on τ_s can not be fully explained by the changes of $\langle b_z^2 \rangle$ and DOS, in particular at relatively low temperature.

We then examine if substrate-induced modifications of phonon can explain the changes of spin relaxation at different substrates, especially at low T. We emphasize that at low T, since spin relaxation is fully determined by intervalley processes (Fig. 2c), the related phonons are mostly close to wavevector K. From Table 1 and Fig. 4, we find that the most important phonon mode for spin relaxation at low T has several similar features: (i) It contributes to more than 60% of spin relaxation (see Table 1). (ii) Its energy is around 7 meV in the table of Table 1. (iii) Its vibration is flexural-like, i.e., atoms mostly vibrate along the out-of-plane direction as shown in Fig. 4a–c. Moreover, for this mode, the substrate atoms have negligible vibration amplitude compared to one of the materials atoms. This is also confirmed in the layer-projected phonon dispersion of ML-Ge-InSe in Fig. 4d. The purple box highlights the critical phonon mode around K, with most contribution from the material layer. (iv) The critical phonon mode does not couple with the substrate strongly, since its vibration frequency does not change much when substrate atoms are fixed (by comparing Fig. 4d with 4e). We thus conclude that the substrate-induced modifications of phonons and thermal vibrations of substrate atoms seem not important for spin relaxation at low T (e.g., below 20 K).

Therefore, neither the simple electronic quantities $\langle b^2 \rangle$ and DOS nor the phonon properties can explain the substrate effects on spin relaxation at low T.

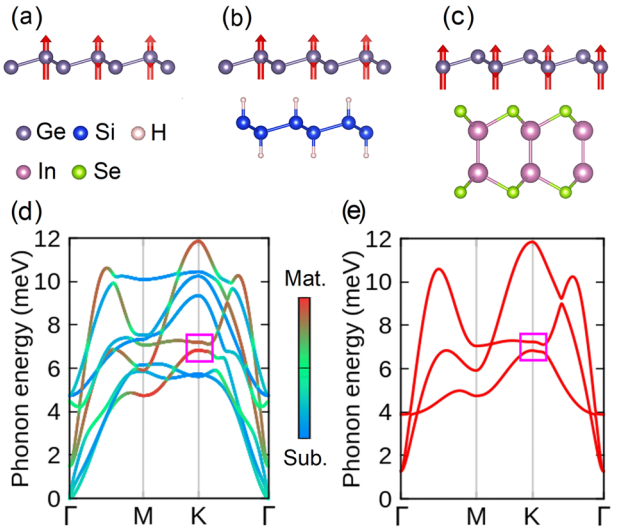

Fig. 4 The analysis of phonons of free-standing and substrate-supported ML-Ge. a–c Typical vibrations of atoms in 3 × 3 supercells of **a** ML-Ge@-7 V/nm, **b** ML-Ge-SiH, and **c** ML-Ge-InSe of the most important phonon mode at K ~7 meV (shown in Table 1). The red arrows represent displacement. The atomic displacements smaller than 10% of the strongest are not shown. **d** The layer-projected phonon dispersion of ML-Ge-InSe within 12 meV. The red and blue colors correspond to the phonon displacements mostly contributed from the material (red) and substrate layer (blue), respectively. The green color means the contribution to the phonon displacements from the material and substrate layers are similar. The purple boxes highlight the two most important phonon modes around K for spin relaxation. **e** Phonon dispersion of ML-Ge-InSe within 12 meV with substrate atoms (InSe) being fixed at equilibrium structure and only Ge atoms are allowed to vibrate.

The determining factors of spin relaxation derived from spin-flip matrix elements

On the other hand, with a simplified picture of spin-flip transition by the Fermi's Golden Rule, the scattering rate is proportional to the modulus square of the scattering matrix elements. For a further mechanistic understanding, we turn to examine the modulus square of the spin-flip matrix elements, and compare their qualitative trend with our FPDM simulations. Note that most matrix elements are irrelevant to spin relaxation and we need to pick the "more relevant" ones, by defining a statistically averaged function. Therefore, we propose an effective band edge-averaged spin-flip matrix element $\overline{|\tilde{g}^{\uparrow\downarrow}|^2}$ (Eq. (8)). Here the spin-flip matrix element can be for general scattering processes; in the following we focus on e-ph process for simplicity. We also propose a so-called scattering density of states D^S in Eq. (9), which measures the density of spin-flip transitions and can be roughly regarded as a weighted-averaged value of the usual DOS. Based on the generalized Fermi's golden rule, we approximately have $\tau_s^{-1} \propto \overline{|\tilde{g}^{\uparrow\downarrow}|^2} D^S$ for EY spin relaxation (see the discussions above Eq. (11) in "Methods" section).

As shown in Fig. 5a, τ_s^{-1} is almost linearly proportional to $\overline{|\tilde{g}^{\uparrow\downarrow}|^2} D^S$ at 20 K. As the variation of D^S among ML-Ge on different substrates is at most three times (see Fig. 3e and Supplementary Fig. 6), which is much weaker than the large variation of τ_s^{-1}, this indicates that the substrate-induced change of τ_s is mostly due to the substrate-induced change of spin-flip matrix elements. Although $\overline{|\tilde{g}^{\uparrow\downarrow}|^2}$ was often considered approximately proportional to $\langle b^2 \rangle$, resulting in $\tau_s^{-1} \propto \langle b^2 \rangle$, our results in Fig. 3 in the earlier section indicate that such simple approximation is not applicable

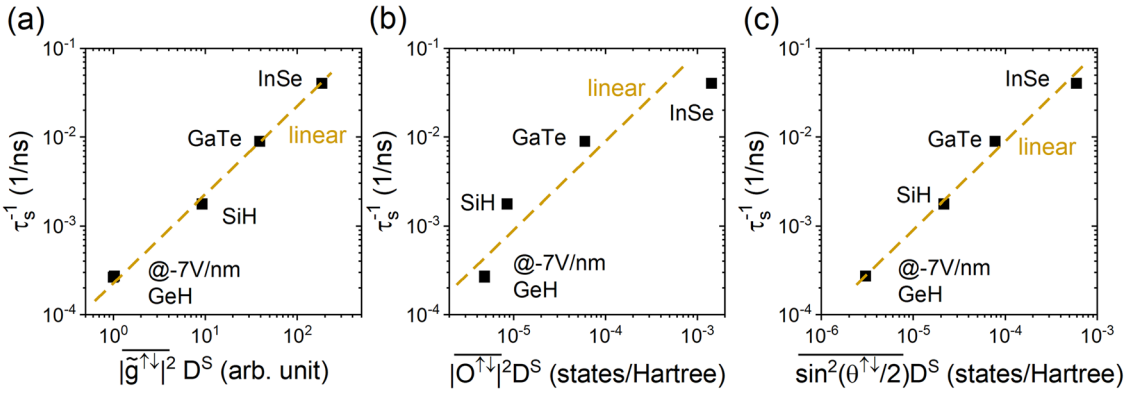

Fig. 5 The relation between τ_s^{-1} and the averaged modulus square of spin-flip e-ph matrix elements $\overline{|\tilde{g}^{\uparrow\downarrow}|^2}$, of spin-flip overlap matrix elements $\overline{|o^{\uparrow\downarrow}|^2}$ and $\overline{\sin^2(\theta^{\uparrow\downarrow}/2)}$ multiplied by the scattering density of states D^S at 20 K. See the definition of $\overline{|\tilde{g}^{\uparrow\downarrow}|^2}$, $\overline{|o^{\uparrow\downarrow}|^2}$ and D^S in Eqs. (8), (19) and (9) respectively. $\theta^{\uparrow\downarrow}$ is the spin-flip angle between two electronic states. For two states (k,n) and (k',n') with opposite spin directions, $\theta^{\uparrow\downarrow}$ is the angle between $-\mathbf{S}^{\rm exp}_{kn}$ and $\mathbf{S}^{\rm exp}_{k'n'}$. $\overline{\sin^2(\theta^{\uparrow\downarrow}/2)}$ is defined in Eq. (24). The variation of D^S among different substrates is at most three times, much weaker than the variations of τ_s^{-1} and other quantities shown here.

here, especially inadequate of explaining substrate dependence of τ_s at low T.

To find out the reason why $\overline{|\tilde{g}^{\uparrow\downarrow}|^2}$ for different substrates are so different, we first examine the averaged spin-flip wavefunction overlap $\overline{|o^{\uparrow\downarrow}|^2}$ (with the reciprocal lattice vector $\mathbf{G}=0$), closely related to $\overline{|\tilde{g}^{\uparrow\downarrow}|^2}$ (Eq. (18) and Eq. (17)). From Fig. 5b, τ_s^{-1} and $\overline{|o^{\uparrow\downarrow}|^2}$ have the same trend, which implies $\overline{|\tilde{g}^{\uparrow\downarrow}|^2}$ and $\overline{|o^{\uparrow\downarrow}|^2}$ may have the same trend. However, in general, the $\mathbf{G}\neq 0$ elements of $\overline{|o^{\uparrow\downarrow}|^2}$ may be important as well, which can not be unambiguously evaluated here. (See detailed discussions in the subsection "Spin-flip e-ph and overlap matrix element" in the "Methods" section).

To have deeper intuitive understanding, we then propose an important electronic quantity for intervalley spin-flip scattering - the spin-flip angle $\theta^{\uparrow\downarrow}$ between two electronic states. For two states (k_1,n_1) and (k_2,n_2) with opposite spin directions, $\theta^{\uparrow\downarrow}$ is the angle between $-\mathbf{S}^{\rm exp}_{k_1n_1}$ and $\mathbf{S}^{\rm exp}_{k_2n_2}$ or equivalently the angle between $-\mathbf{B}^{\rm in}_{k_1}$ and $\mathbf{B}^{\rm in}_{k_2}$.

The motivation of examining $\theta^{\uparrow\downarrow}$ is that: Suppose two wavevectors $\mathbf{k}_1$ and $\mathbf{k}_2=-\mathbf{k}_1$ are in two opposite valleys Q and $-Q$ respectively and there is a pair of bands, which are originally Kramers degenerate but splitted by $\mathbf{B}^{\rm in}$. Due to time-reversal symmetry, we have $\mathbf{B}^{\rm in}_{k_1}=-\mathbf{B}^{\rm in}_{k_2}$, which means the two states at the same band n at $\mathbf{k}_1$ and $\mathbf{k}_2$ have opposite spins and $\theta^{\uparrow\downarrow}$ between them is zero. Therefore, the matrix element of operator $\hat{A}$ between states (k_1,n) and (k_2,n) - A_{k_1n,k_2n} is a spin-flip one and we name it as $A^{\uparrow\downarrow}_{k_1k_2}$. According to ref. [27], with time-reversal symmetry, $A^{\uparrow\downarrow}_{k_1k_2}$ is exactly zero. In general, for another wavevector $\mathbf{k}_3$ within valley $-Q$ but not $-\mathbf{k}_1$, $A^{\uparrow\downarrow}_{k_1k_3}$ is usually non-zero. One critical quantity that determines the intervalley spin-flip matrix element $A^{\uparrow\downarrow}_{k_1k_3}$ for a band within the pair introduced above is $\theta^{\uparrow\downarrow}_{k_1k_3}$. Based on time-independent perturbation theory, we can prove that $|A^{\uparrow\downarrow}|$ between two states is approximately proportional to $|\sin(\theta^{\uparrow\downarrow}/2)|$. The derivation is given in subsection "Spin-flip angle $\theta^{\uparrow\downarrow}$ for intervalley spin relaxation in "Methods" section.

As shown in Fig. 5c, τ_s^{-1} of ML-Ge on different substrates at 20 K is almost linearly proportional to $\overline{\sin^2(\theta^{\uparrow\downarrow}/2)}D^S$, where $\overline{\sin^2(\theta^{\uparrow\downarrow}/2)}$ is the statistically averaged modulus square of $\sin(\theta^{\uparrow\downarrow}/2)$. This indicates that the relation $\overline{|\tilde{g}^{\uparrow\downarrow}|^2}\propto\overline{\sin^2(\theta^{\uparrow\downarrow}/2)}$ is nearly perfectly satisfied at low T, where intervalley processes dominate spin relaxation. We additionally show the relations between τ_s^{-1} and $\overline{|\tilde{g}^{\uparrow\downarrow}|^2}D^S$, $\overline{|o^{\uparrow\downarrow}|^2}D^S$ and $\overline{\sin^2(\theta^{\uparrow\downarrow}/2)}D^S$ at 300 K in Supplementary Fig. 7. Here the trend of τ_s^{-1} is still approximately captured by the trends of $\overline{|\tilde{g}^{\uparrow\downarrow}|^2}D^S$, $\overline{|o^{\uparrow\downarrow}|^2}D^S$ and $\overline{\sin^2(\theta^{\uparrow\downarrow}/2)}D^S$, although not perfectly linear as at low T.

Since $\theta^{\uparrow\downarrow}$ is defined by $\mathbf{S}^{\rm exp}$ at different states, τ_s is highly correlated with $\mathbf{S}^{\rm exp}$ and more specifically with the anisotropy of $\mathbf{S}^{\rm exp}$ (equivalent to the anisotropy of $\mathbf{B}^{\rm in}$). Qualitatively, the larger anisotropy of $\mathbf{S}^{\rm exp}$ leads to smaller $\theta^{\uparrow\downarrow}$ and longer τ_s along the high-spin-polarization direction. This finding may be applicable to spin relaxation in other materials whenever intervalley spin-flip scattering dominates or spin-valley locking exists, e.g., in TMDs[5], Stanene[28], 2D hybrid perovskites with persistent spin helix[7], etc.

Finally, we briefly discuss the substrate effects on in-plane spin relaxation ($\tau_{s,x}$), whereas only out-of-plane spin relaxation was discussed earlier. From Supplementary Table 1, we find that $\tau_{s,x}$ of ML-Ge@-7 V/nm and supported ML-Ge are significantly (e.g., two orders of magnitude) shorter than free-standing ML-Ge, but the differences between $\tau_{s,x}$ of ML-Ge on different substrates are relatively small (within 50%). This is because: With a non-zero E_z or a substrate, the inversion symmetry broken induces strong out-of-plane internal magnetic field $B^{\rm in}_z$ (>100 Tesla), so that the excited in-plane spins will precess rapidly about $B^{\rm in}_z$. The spin precession significantly affects spin decay and the main spin decay mechanism becomes DP or free induction decay mechanism[29] instead of EY mechanism. For both DP and free induction decay mechanisms[21,29], $\tau_{s,x}$ decreases with the fluctuation amplitude (among different k-points) of the $\mathbf{B}^{\rm in}$ components perpendicular to the x direction. As the fluctuation amplitude of $B^{\rm in}_z$ of ML-Ge@-7 V/nm and supported ML-Ge is large (Supplementary Table 1; much greater than the one of $B^{\rm in}_y$), their $\tau_{s,x}$ can be much shorter than the value of ML-Ge at zero electric field when EY mechanism dominates. Moreover, since the fluctuation amplitude of $B^{\rm in}_z$ of ML-Ge on different substrates has the same order of magnitude (Supplementary Table 1), $\tau_{s,x}$ of ML-Ge on different substrates are similar.

DISCUSSION

In summary, we systematically investigate how to spin relaxation of strong SOC Dirac materials is affected by different insulating substrates, using germanene as a prototypical example. Through FPDM simulations of τ_s of free-standing and substrate-supported ML-Ge, we show that substrate effects on τ_s can differ orders of magnitude among different substrates. Specifically, τ_s of ML-Ge-GeH and ML-Ge-SiH have the same order of magnitude as

free-standing ML-Ge, but τ_s of ML-Ge-GaTe and ML-Ge-InSe are significantly shortened by 1-2 orders with temperature increasing from 20 K to 300 K.

Although simple electronic quantities including charge densities, DOS, and spin mixing $\langle b_z^2 \rangle$ qualitatively explain the much shorter lifetime of ML-Ge-GaTe/InSe compared to ML-Ge-GeH/SiH in the relatively high T range, we find they cannot explain the large variations of τ_s among substrates at low T (i.e., tens of K). We point out that spin relaxation in ML-Ge and its interfaces at low T is dominated by intervalley scattering processes. However, the substrate-induced modifications of phonons and thermal vibrations of substrates seem to be not important. Instead, the substrate-induced changes of the anisotropy of $\mathbf{S}^{\text{exp}}$ or the spin-flip angles $\theta^{\uparrow\downarrow}$ which changes the spin-flip matrix elements, are much more crucial. $\theta^{\uparrow\downarrow}$ is at the first time proposed in this article to the best of our knowledge, and is found to be a useful electronic quantity for predicting trends of spin relaxation when intervalley spin-flip scattering dominates.

Our theoretical study showcases the systematic investigations of the critical factors determining the spin relaxation in 2D Dirac materials. More importantly, we pointed out the sharp distinction of substrate effects on strong SOC materials to the effects on weak SOC ones, providing valuable insights and guidelines for optimizing spin relaxation in materials synthesis and control.

METHODS

First-principles density-matrix dynamics for spin relaxation

We solve the quantum master equation of density-matrix $\rho(t)$ as the following[20]:

$$\frac{d\rho_{12}(t)}{dt} = -\frac{i}{\hbar}[H_e, \rho(t)]_{12} + \left(\begin{array}{c} \frac{1}{2}\sum_{345} \left\{ \begin{array}{c} [I-\rho(t)]_{13} P_{32,45} \rho_{45}(t) \\ -[I-\rho(t)]_{45} P^*_{45,13} \rho_{32}(t) \end{array} \right\} \\ +H.C. \end{array} \right), \tag{1}$$

Eq. (1) is expressed in the Schrödinger picture, where the first and second terms on the right side of the equation relate to the coherent dynamics, which can lead to Larmor precession, and scattering processes respectively. The first term is unimportant for out-of-plane spin relaxation in ML-Ge systems, since Larmor precession is highly suppressed for the excited spins along the out-of-plane or z direction due to high-spin polarization along z direction. The scattering processes induce spin relaxation via the SOC. H_e is the electronic Hamiltonian. $[H, \rho] = H\rho - \rho H$. H.C. is Hermitian conjugate. The subindex, e.g., "1" is the combined index of $\mathbf{k}$-point and band. $P = P^{\text{e-ph}} + P^{\text{e-i}}$ is the generalized scattering-rate matrix considering e-ph and e-i scattering processes.

For the e-ph scattering[20],

$$P^{\text{e-ph}}_{1234} = \sum_{q\lambda\pm} A^{q\lambda\pm}_{13} A^{q\lambda\pm,*}_{24}, \tag{2}$$

$$A^{q\lambda\pm}_{13} = \sqrt{\frac{2\pi}{\hbar}} g^{q\lambda\pm}_{12} \sqrt{\delta^G_\sigma(\epsilon_1 - \epsilon_2 \pm \omega_{q\lambda})} \sqrt{n^{\pm}_{q\lambda}}, \tag{3}$$

where q and λ are phonon wavevector and mode, $g^{q\lambda\pm}$ is the e-ph matrix element, resulting from the absorption $(-)$ or emission $(+)$ of a phonon, computed with self-consistent SOC from first-principles[30], $n^{\pm}_{q\lambda} = n_{q\lambda} + 0.5 \pm 0.5$ in terms of phonon Bose factors $n_{q\lambda}$, and δ^G_σ represents an energy conserving δ-function broadened to a Gaussian of width σ.

For electron-impurity scattering[20],

$$P^{\text{e-i}}_{1234} = A^i_{13} A^{i,*}_{24}, \tag{4}$$

$$A^i_{13} = \sqrt{\frac{2\pi}{\hbar}} g^i_{13} \sqrt{\delta^G_\sigma(\epsilon_1 - \epsilon_3)} \sqrt{n_i V_{\text{cell}}}, \tag{5}$$

where n_i and V_{cell} are impurity density and unit cell volume, respectively. g^i is the e-i matrix element computed by the supercell method and is discussed in the next subsection.

Starting from an initial density-matrix $\rho(t_0)$ prepared with a net spin, we evolve $\rho(t)$ through Eq. (1) for a long enough time, typically from hundreds of ps to a few μs. We then obtain spin observable $S(t)$ from $\rho(t)$ (Supplementary Equation 1) and extract spin lifetime τ_s from $S(t)$ using Supplementary Equation 2.

Computational details

The ground-state electronic structure, phonons, as well as electron-phonon and electron-impurity (e-i) matrix elements are firstly calculated using density functional theory (DFT) with relatively coarse k and q meshes in the DFT plane-wave code JDFTx[31]. Since all substrates have hexagonal structures and their lattice constants are close to germanene's, the heterostructures are built simply from unit cells of two systems. The lattice mismatch values are within 1% for GeH, GaTe, and InSe substrates but ~3.5% for the SiH substrate. All heterostructures use the lattice constant 4.025 Å of free-standing ML-Ge relaxed with Perdew-Burke-Ernzerhof exchange-correlation functional[32]. The internal geometries are fully relaxed using the DFT+D3 method for van der Waals dispersion corrections[33]. We use Optimized Norm-Conserving Vanderbilt (ONCV) pseudopotentials[34] with self-consistent spin-orbit coupling throughout, which we find converged at a kinetic energy cutoff of 44, 64, 64, 72, and 66 Ry for free-standing ML-Ge, ML-Ge-GeH, ML-Ge-SiH, ML-Ge-GaTe, and ML-Ge-InSe respectively. The DFT calculations use 24×24 k meshes. The phonon calculations employ 3×3 supercells through finite difference calculations. We have checked the supercell size convergence and found that using 6×6 supercells lead to very similar results of phonon dispersions and spin lifetimes. For all systems, the Coulomb truncation technique[35] is employed to accelerate convergence with vacuum sizes. The vacuum sizes are 20 bohr (additional to the thickness of the heterostructures) for all heterostructures and are found large enough to converge the final results of spin lifetimes. The electric field along the non-periodic direction is applied as a ramp potential.

For the e-i scattering, we assume impurity density is sufficiently low and the average distance between neighboring impurities is sufficiently long so that the interactions between impurities are negligible, i.e., at the dilute limit. The e-i matrix g^i between state (k, n) and (k', n') is $g^i_{kn,k'n'} = \langle kn|V^i - V^0|k'n'\rangle$, where V^i is the potential of the impurity system and V^0 is the potential of the pristine system. V^i is computed with SOC using a large supercell including a neutral impurity that simulates the dilute limit where impurity and its periodic replica do not interact. To speed up the supercell convergence, we used the potential alignment method developed in ref. [36]. We use 5×5 supercells, which have shown reasonable convergence (a few percent error of the spin lifetime).

We then transform all quantities from plane-wave basis to maximally localized Wannier function basis[37], and interpolate them[30,38–42] to substantially finer k and q meshes. The fine k and q meshes are 384×384 and 576×576 for simulations at 300 K and 100 K respectively and are finer at lower temperature, e.g., 1440×1440 and 2400×2400 for simulations at 50 K and 20 K respectively.

The real-time dynamics simulations are done with our own developed DMD code interfaced to JDFTx. We evolve $\rho(t)$ through Eq. (1) using an adaptive Runge-Kutta fourth-order method, where the time step dt is controlled automatically to be small enough to ensure the errors of $\rho(t)$ tiny. Typically, dt ranges from 0.1 fs to 10 ps depending on specific materials, temperature, external field, impurity densities, etc. In this work, dt ranges from 10 fs to 1 ps. The energy-conservation smearing parameter σ is chosen to be comparable or smaller than k_BT for each calculation, e.g., 10 meV,

5 meV, 3.3 meV and 1.3 meV at 300 K, 100 K, 50 K, and 20 K respectively.

Analysis of Elliot-Yafet spin lifetime

In order to analyze the results from real-time first-principles density-matrix dynamics (FPDM), we compare them with simplified mechanistic models as discussed below. According to ref. [19], if a solid-state system is close to equilibrium (but not at equilibrium) and its spin relaxation is dominated by EY mechanism, its spin lifetime τ_s due to the e-ph scattering satisfies (for simplicity the band indices are dropped)

$$\tau_s^{-1} \propto \frac{N_k^{-2}}{\chi}\sum_{kq\lambda}\left\{\begin{array}{c}|g^{\uparrow\downarrow,q\lambda}_{k,k-q}|^2 n_{q\lambda} f_{k-q}(1-f_k)\\ \delta(\epsilon_k-\epsilon_{k-q}-\omega_{q\lambda})\end{array}\right\}, \tag{6}$$

$$\chi = N_k^{-1}\sum_k f_k(1-f_k), \tag{7}$$

where f is Fermi-Dirac function. $\omega_{q\lambda}$ and $n_{q\lambda}$ are phonon energy and occupation of phonon mode λ at wavevector q. $g^{\uparrow\downarrow}$ is the spin-flip e-ph matrix element between two electronic states of opposite spins. We will further discuss $g^{\uparrow\downarrow}$ in the next subsection.

According to Eqs. (6) and (7), τ_s^{-1} is proportional to $|g_q^{\uparrow\downarrow}|^2$ and also the density of the spin-flip transitions. Therefore we propose a temperature (T) and chemical potential dependent effective modulus square of the spin-flip e-ph matrix element $\overline{|\tilde{g}^{\uparrow\downarrow}|^2}$ and a scattering density of states D^S as

$$\overline{|\tilde{g}^{\uparrow\downarrow}|^2} = \frac{\sum_{kq} w_{k,k-q}\sum_\lambda |g^{\uparrow\downarrow,q\lambda}_{k,k-q}|^2 n_{q\lambda}}{\sum_{kq} w_{k,k-q}}, \tag{8}$$

$$D^S = \frac{N_k^{-2}\sum_{kq} w_{k,k-q}}{N_k^{-1}\sum_k f_k(1-f_k)}, \tag{9}$$

$$w_{k,k-q} = f_{k-q}(1-f_k)\delta(\epsilon_k-\epsilon_{k-q}-\omega_c), \tag{10}$$

where ω_c is the characteristic phonon energy specified below, and $w_{k,k-q}$ is the weight function. The matrix element modulus square is weighted by $n_{q\lambda}$ according to Eqs. (6) and (7). This rules out high-frequency phonons at low T which are not excited. ω_c is chosen as 7 meV at 20 K based on our analysis of phonon mode-resolved contribution to spin relaxation. $w_{k,k-q}$ selects transitions between states separated by ω_c and around the band edge or chemical potential, which are "more relevant" transitions to spin relaxation.

D^S can be regarded as an effective density of spin-flip e-ph transitions satisfying energy-conservation between one state and its pairs. When $\omega_c = 0$, we have $D^S = \int d\epsilon\left(-\frac{df}{d\epsilon}\right)D^2(\epsilon)/\int d\epsilon\left(-\frac{df}{d\epsilon}\right)D(\epsilon)$ with $D(\epsilon)$ density of electronic states (DOS). So D^S can be roughly regarded as a weighted-averaged DOS with weight $\left(-\frac{df}{d\epsilon}\right)D(\epsilon)$.

With $\overline{|\tilde{g}^{\uparrow\downarrow}|^2}$ and D^S, we have the approximate relation for spin relaxation rate,

$$\tau_s^{-1} \propto \overline{|\tilde{g}^{\uparrow\downarrow}|^2} D^S. \tag{11}$$

Spin-flip e-ph and overlap matrix element

In the mechanistic model of Eq. (6) in the last section, the spin-flip e-ph matrix element between two electronic states of opposite spins at wavevectors $\mathbf{k}$ and $\mathbf{k}$ - $\mathbf{q}$ of phonon mode λ reads[30]

$$g^{\uparrow\downarrow,q\lambda}_{kk-q} = \left\langle u_k^{\uparrow(\downarrow)}\middle|\Delta_{q\lambda}v^{KS}\middle|u_{k-q}^{\downarrow(\uparrow)}\right\rangle, \tag{12}$$

$$\Delta_{q\lambda}v^{KS} = \sqrt{\frac{\hbar}{2\omega_{q\lambda}}}\sum_{\kappa\alpha}\frac{e_{\kappa\alpha,q\lambda}\partial_{\kappa\alpha q}v^{KS}}{\sqrt{m_\kappa}}, \tag{13}$$

$$\partial_{\kappa\alpha q}v^{KS} = \sum_l e^{i\mathbf{q}\cdot\mathbf{R}_l}\frac{\partial V^{KS}}{\partial\tau_{\kappa\alpha}}|_{\mathbf{r}-\mathbf{R}_l}, \tag{14}$$

$$V^{KS} = +\frac{\hbar}{4m^2c^2}\nabla_{\mathbf{r}}V\times\mathbf{p}\cdot\sigma, \tag{15}$$

where $u_k^{\uparrow(\downarrow)}$ is the periodic part of the Bloch wavefunction of a spin-up (spin-down) state at wavevector $\mathbf{k}$. κ is the index of ion in the unit cell. α is the index of a direction. $\mathbf{R}_l$ is a lattice vector. V is the spin-independent part of the potential. $\mathbf{p}$ is the momentum operator. σ is the Pauli operator.

From Eqs. (12)–(15), $g^{\uparrow\downarrow}$ can be separated into two parts,

$$g^{\uparrow\downarrow} = g^E + g^Y, \tag{16}$$

where g^E and g^Y correspond to the spin-independent and spin-dependent parts of V^{KS} respectively, called Elliot and Yafet terms of the spin-flip scattering matrix elements respectively[29].

Generally speaking, both the Elliot and Yafet terms are important; for the current systems τ_s with and without Yafet term have the same order of magnitude. For example, τ_s of ML-Ge-GeH and ML-Ge-SiH without the Yafet term are about 100% and 70% of τ_s with the Yafet term at 20 K. Therefore, for qualitative discussion of τ_s of ML-Ge on different substrates (the quantitative calculations of τ_s are performed by FPDM introduced earlier), it is reasonable to focus on the Elliot term g^E and avoid the more complicated Yafet term g^Y.

Define $V^E_{q\lambda}$ as the spin-independent part of $\Delta_{q\lambda}v^{KS}$, so that $g^E = \left\langle u_k^{\uparrow(\downarrow)}\middle|V^E_{q\lambda}\middle|u_{k-q}^{\downarrow(\uparrow)}\right\rangle$. Expanding $V^E_{q\lambda}$ as $\sum_G \tilde{V}^E_{q\lambda}(\mathbf{G})e^{i\mathbf{G}\cdot\mathbf{r}}$, we have

$$g^E = \sum_G \tilde{V}^E_{q\lambda}(\mathbf{G})o^{\uparrow\downarrow}_{kk-q}(\mathbf{G}), \tag{17}$$

$$o^{\uparrow\downarrow}_{kk-q}(\mathbf{G}) = \left\langle u_k^{\uparrow(\downarrow)}\middle|e^{i\mathbf{G}\cdot\mathbf{r}}\middle|u_{k-q}^{\downarrow(\uparrow)}\right\rangle, \tag{18}$$

where $o^{\uparrow\downarrow}_{kk-q}(\mathbf{G})$ is $\mathbf{G}$-dependent spin-flip overlap function. Without loss of generality, we suppose the first Brillouin zone is centered at Γ.

Therefore, g^E is not only determined by the long-range component of $o^{\uparrow\downarrow}_{kk-q}(\mathbf{G})$, i.e., $o^{\uparrow\downarrow}_{kk-q}(\mathbf{G}=0)$ but also the $\mathbf{G}\neq 0$ components. The $\mathbf{G}\neq 0$ components can be important but cannot be unambiguously evaluated. Nevertheless, it is helpful to investigate $o^{\uparrow\downarrow}_{kk-q}(\mathbf{G}=0)$ and similar to Eq. (8), we propose an effective modulus square of the spin-flip overlap matrix element $\overline{|o^{\uparrow\downarrow}|^2}$,

$$\overline{|o^{\uparrow\downarrow}|^2} = \frac{\sum_{kq} w_{k,k-q}\sum_\lambda |o^{\uparrow\downarrow}_{k,k-q}(\mathbf{G}=0)|^2}{\sum_{kq} w_{k,k-q}}. \tag{19}$$

Internal magnetic field

Suppose originally a system has time-reversal and inversion symmetries, so that every two bands form a Kramers degenerate pair. Suppose the $\mathbf{k}$-dependent spin matrix vectors in Bloch basis of the Kramers degenerate pairs are $\mathbf{s}^0_k$ with $\mathbf{s}\equiv(s_x,s_y,s_z)$. The inversion symmetry broken, possibly due to applying an electric field or a substrate, induces $\mathbf{k}$-dependent Hamiltonian terms

$$H^{ISB}_k = \mu_B g_e \mathbf{B}^{in}_k\cdot\mathbf{s}^0_k, \tag{20}$$

where $\mu_B g_e$ is the electron spin gyromagnetic ratio. $\mathbf{B}^{in}_k$ is the SOC-field and called internal magnetic fields. $\mathbf{B}^{in}$ splits the degenerate

pair and polarizes the spin along its direction. The definition of $\mathbf{B}_k^{\text{in}}$ is

$$\mathbf{B}_k^{\text{in}} \equiv 2\Delta_k^{\text{SOC}}\mathbf{S}_k^{\text{exp}}/(\mu_B g_e), \tag{21}$$

where $\mathbf{S}^{\text{exp}} \equiv \left(S_x^{\text{exp}}, S_y^{\text{exp}}, S_z^{\text{exp}}\right)$ with S_i^{exp} being spin expectation value along direction i and is the diagonal element of s_i. Δ^{SOC} is the band splitting energy by SOC.

Spin-flip angle $\theta^{\uparrow\downarrow}$ for intervalley spin relaxation

Suppose (i) the inversion symmetry broken induces $\mathbf{B}_k^{\text{in}}$ (Eq. (21)) for a Kramers degenerate pair; (i) there are two valleys centered at wavevectors $\mathbf{Q}$ and $-\mathbf{Q}$ and (iii) there are two wavevectors $\mathbf{k}_1$ and $\mathbf{k}_2$ near $\mathbf{Q}$ and $-\mathbf{Q}$ respectively. Due to time-reversal symmetry, the directions of $\mathbf{B}_{k_1}^{\text{in}}$ and $\mathbf{B}_{k_2}^{\text{in}}$ are almost opposite.

Define the spin-flip angle $\theta_{k_1k_2}^{\uparrow\downarrow}$ as the angle between $-\mathbf{B}_{k_1}^{\text{in}}$ and $\mathbf{B}_{k_2}^{\text{in}}$, which is also the angle between $-\mathbf{S}_{k_1}^{\text{exp}}$ and $\mathbf{S}_{k_2}^{\text{exp}}$. We will prove that for a general operator $\widehat{A}$,

$$\left|A_{k_1k_2}^{\uparrow\downarrow}\right|^2 \approx \sin^2\left(\theta_{k_1k_2}^{\uparrow\downarrow}/2\right)\left|A_{k_1k_2}^{\downarrow\downarrow}\right|^2, \tag{22}$$

where $A_{k_1k_2}^{\uparrow\downarrow}$ and $A_{k_1k_2}^{\downarrow\downarrow}$ are the spin-flip and spin-conserving matrix elements between $\mathbf{k}_1$ and $\mathbf{k}_2$ respectively.

The derivation uses the first-order perturbation theory and has three steps:

Step 1: The 2×2 matrix of operator $\widehat{A}$ between $\mathbf{k}_1$ and $\mathbf{k}_2$ of two Kramers degenerate bands is $A_{k_1k_2}^0$. According to ref. [27], with time-reversal symmetry, the spin-flip matrix element of the same band between $\mathbf{k}$ and $-\mathbf{k}$ is exactly zero, therefore, the spin-flip matrix elements of $A_{k_1k_2}^0$ are zero at lowest order as $\mathbf{k}_1+\mathbf{k}_2\approx0$, i.e., $A_{k_1k_2}^{0,\uparrow\downarrow} \approx A_{k_1k_2}^{0,\downarrow\uparrow} \approx 0$.

Step 2: The inversion symmetry broken induces $\mathbf{B}_k^{\text{in}}$ and the perturbed Hamiltonian H_k^{ISB} (Eq. (20)). The new eigenvectors U_k are obtained based on the first-order perturbation theory.

Step 3: The new matrix is $A_{k_1k_2} = U_{k_1}^\dagger A_{k_1k_2}^0 U_{k_2}$. Thus the spin-flip matrix elements $A_{k_1k_2}^{\uparrow\downarrow}$ with the inversion symmetry broken are obtained.

We present the detailed derivation in Supplementary Note 4.

From Eq. (22), for the intervalley e-ph matrix elements of ML-Ge systems, we have

$$\left|g_{k_1k_2}^{\uparrow\downarrow}\right|^2 \approx \sin^2\left(\theta_{k_1k_2}^{\uparrow\downarrow}/2\right)\left|g_{k_1k_2}^{\downarrow\downarrow}\right|^2. \tag{23}$$

As $|g_{k_1k_2}^{\uparrow\downarrow}|^2$ largely determines τ_s of ML-Ge systems, the differences of τ_s of ML-Ge on different substrates should be mainly due to the difference of $\sin^2(\theta_{k_1k_2}^{\uparrow\downarrow}/2)$.

For the intervalley overlap matrix elements, we should have $\left|o_{k_1k_2}^{\uparrow\downarrow}\right|^2 \approx \sin^2\left(\theta_{k_1k_2}^{\uparrow\downarrow}/2\right)\left|o_{k_1k_2}^{\downarrow\downarrow}\right|^2$. Since $\left|o_{k_1k_2}^{\downarrow\downarrow}\right|^2$ is of order 1, $\left|o_{k_1k_2}^{\uparrow\downarrow}\right|^2$ is expected proportional to $\sin^2\left(\theta_{k_1k_2}^{\uparrow\downarrow}/2\right)$ and have the same order of magnitude as $\sin^2\left(\theta_{k_1k_2}^{\uparrow\downarrow}/2\right)$.

Finally, similar to Eq. (8), we propose an effective modulus square of $\sin^2(\theta_{k_1k_2}^{\uparrow\downarrow}/2)$,

$$\overline{\sin^2\left(\theta^{\uparrow\downarrow}/2\right)} = \frac{\sum_{kq} w_{k,k-q}\sin^2\left(\theta_{k,k-q}^{\uparrow\downarrow}/2\right)}{\sum_{kq} w_{k,k-q}}. \tag{24}$$

DATA AVAILABILITY

The data that support the findings of this study are available upon request to the corresponding author.

CODE AVAILABILITY

The codes that were used in this study are available upon request to the corresponding author.

Received: 20 June 2022; Accepted: 6 March 2023;
Published online: 31 March 2023

REFERENCES

1. Tombros, N., Jozsa, C., Popinciuc, M., Jonkman, H. T. & Van Wees, B. J. Electronic spin transport and spin precession in single graphene layers at room temperature. *Nature* **448**, 571–574 (2007).
2. Avsar, A. et al. Colloquium: spintronics in graphene and other two-dimensional materials. *Rev. Mod. Phys.* **92**, 021003 (2020).
3. Drogeler, M. et al. Spin lifetimes exceeding 12 ns in graphene nonlocal spin valve devices. *Nano Lett.* **16**, 3533–3539 (2016).
4. Avsar, A. et al. Gate-tunable black phosphorus spin valve with nanosecond spin lifetimes. *Nat. Phys.* **13**, 888–893 (2017).
5. Dey, P. et al. Gate-controlled spin-valley locking of resident carriers in WSe2 monolayers. *Phys. Rev. Lett.* **119**, 137401 (2017).
6. Xu, J., Takenaka, H., Habib, A., Sundararaman, R. & Ping, Y. Giant spin lifetime anisotropy and spin-valley locking in silicene and germanene from first-principles density-matrix dynamics. *Nano Lett.* **21**, 9594–9600 (2021).
7. Zhang, L. et al. Room-temperature electrically switchable spin–valley coupling in a van der waals ferroelectric halide perovskite with persistent spin helix. *Nat. Photon.* **16**, 529–537 (2022).
8. Koralek, J. D. et al. Emergence of the persistent spin helix in semiconductor quantum wells. *Nature* **458**, 610–613 (2009).
9. Habib, A., Xu, J., Ping, Y. & Sundararaman, R. Electric fields and substrates dramatically accelerate spin relaxation in graphene. *Phys. Rev. B* **105**, 115122 (2022).
10. Ertler, C., Konschuh, S., Gmitra, M. & Fabian, J. Electron spin relaxation in graphene: the role of the substrate. *Phys. Rev. B* **80**, 041405 (2009).
11. Cummings, A. W., Garcia, J. H., Fabian, J. & Roche, S. Giant spin lifetime anisotropy in graphene induced by proximity effects. *Phys. Rev. Lett.* **119**, 206601 (2017).
12. Van Tuan, D., Ortmann, F., Cummings, A. W., Soriano, D. & Roche, S. Spin dynamics and relaxation in graphene dictated by electron-hole puddles. *Sci. Rep.* **6**, 1–8 (2016).
13. Zhang, P. & Wu, M. Electron spin relaxation in graphene with random rashba field: comparison of the d'yakonov–perel'and elliott–yafet-like mechanisms. *N. J. Phys.* **14**, 033015 (2012).
14. Li, J. et al. Valley relaxation of resident electrons and holes in a monolayer semiconductor: dependence on carrier density and the role of substrate-induced disorder. *Phys. Rev. Mater.* **5**, 044001 (2021).
15. Ni, Z., Minamitani, E., Ando, Y. & Watanabe, S. The electronic structure of quasi-free-standing germanene on monolayer mx (m= ga, in; x= s, se, te). *Phys. Chem. Chem. Phys.* **17**, 19039–19044 (2015).
16. Amlaki, T., Bokdam, M. & Kelly, P. J. Z_2 invariance of germanene on mos_2 from first principles. *Phys. Rev. Lett.* **116**, 256805 (2016).
17. Zollner, K., Cummings, A. W., Roche, S. & Fabian, J. Graphene on two-dimensional hexagonal bn, aln, and gan: electronic, spin-orbit, and spin relaxation properties. *Phys. Rev. B* **103**, 075129 (2021).
18. Žutić, I., Fabian, J. & Sarma, S. D. Spintronics: fundamentals and applications. *Rev. Mod. Phys.* **76**, 323 (2004).
19. Xu, J. et al. Spin-phonon relaxation from a universal ab initio density-matrix approach. *Nat. Commun.* **11**, 2780 (2020).
20. Xu, J., Habib, A., Sundararaman, R. & Ping, Y. Ab initio ultrafast spin dynamics in solids. *Phys. Rev. B* **104**, 184418 (2021).
21. Xu, J. et al. How spin relaxes in bulk halide perovskites. https://arxiv.org/abs/2210.17074 (2022).
22. Giousis, T. et al. Synthesis of 2d germanane (geh): a new, fast, and facile approach. *Angew. Chem.* **133**, 364–369 (2021).
23. Lei, S. et al. Evolution of the electronic band structure and efficient photodetection in atomic layers of inse. *ACS Nano* **8**, 1263–1272 (2014).
24. Padilha, J. E. & Pontes, R. B. Electronic and transport properties of structural defects in monolayer germanene: an ab initio investigation. *Solid State Commun.* **225**, 38–43 (2016).
25. Ali, M., Pi, X., Liu, Y. & Yang, D. Electronic and magnetic properties of graphene, silicene and germanene with varying vacancy concentration. *AIP Adv.* **7**, 045308 (2017).
26. Kochan, D., Irmer, S. & Fabian, J. Model spin-orbit coupling hamiltonians for graphene systems. *Phys. Rev. B* **95**, 165415 (2017).
27. Yafet, Y. g factors and spin-lattice relaxation of conduction electrons. *Solid State Phys.* **14**, 1–98 (1963).

28. Tao, L. & Tsymbal, E. Y. Two-dimensional spin-valley locking spin valve. *Phys. Rev. B* **100**, 161110 (2019).
29. Wu, M., Jiang, J. & Weng, M. Spin dynamics in semiconductors. *Phys. Rep.* **493**, 61–236 (2010).
30. Giustino, F. Electron-phonon interactions from first principles. *Rev. Mod. Phys.* **89**, 015003 (2017).
31. Sundararaman, R. et al. JDFTx: software for joint density-functional theory. *SoftwareX* **6**, 278–284 (2017).
32. Perdew, J. P., Burke, K. & Ernzerhof, M. Generalized gradient approximation made simple. *Phys. Rev. Lett.* **77**, 3865 (1996).
33. Grimme, S., Antony, J., Ehrlich, S. & Krieg, H. A consistent and accurate ab initio parametrization of density functional dispersion correction (dft-d) for the 94 elements h-pu. *J. Chem. Phys.* **132**, 154104 (2010).
34. Hamann, D. R. Optimized norm-conserving vanderbilt pseudopotentials. *Phys. Rev. B* **88**, 085117 (2013).
35. Ismail-Beigi, S. Truncation of periodic image interactions for confined systems. *Phys. Rev. B* **73**, 233103 (2006).
36. Sundararaman, R. & Ping, Y. First-principles electrostatic potentials for reliable alignment at interfaces and defects. *J. Chem. Phys.* **146**, 104109 (2017).
37. Marzari, N. & Vanderbilt, D. Maximally localized generalized wannier functions for composite energy bands. *Phys. Rev. B* **56**, 12847 (1997).
38. Brown, A. M., Sundararaman, R., Narang, P., Goddard, W. A. & Atwater, H. A. Nonradiative plasmon decay and hot carrier dynamics: effects of phonons, surfaces, and geometry. *ACS Nano* **10**, 957–966 (2016).
39. Narang, P., Zhao, L., Claybrook, S. & Sundararaman, R. Effects of interlayer coupling on hot carrier dynamics in graphene-derived van der waals heterostructures. *Adv. Opt. Mater.* **5**, 1600914 (2017).
40. Brown, A. M. et al. Experimental and Ab initio ultrafast carrier dynamics in plasmonic nanoparticles. *Phys. Rev. Lett.* **118**, 087401 (2017).
41. Habib, A., Florio, R. & Sundararaman, R. Hot carrier dynamics in plasmonic transition metal nitrides. *J. Opt.* **20**, 064001 (2018).
42. Brown, A. M., Sundararaman, R., Narang, P., Goddard III, W. A. & Atwater, H. A. Ab initio phonon coupling and optical response of hot electrons in plasmonic metals. *Phys. Rev. B* **94**, 075120 (2016).
43. Towns, J. et al. XSEDE: accelerating scientific discovery. *Comput. Sci. Eng.* **16**, 62–74 (2014).

ACKNOWLEDGEMENTS

We thank Ravishankar Sundararaman for helpful discussions. This work is supported by the Air Force Office of Scientific Research under AFOSR Award No. FA9550-21-1-0087. This research used resources of the Center for Functional Nanomaterials, which is a US DOE Office of Science Facility, and the Scientific Data and Computing center, a component of the Computational Science Initiative, at Brookhaven National Laboratory under Contract No. DE-SC0012704, the lux supercomputer at UC Santa Cruz, funded by NSF MRI grant AST 1828315, the National Energy Research Scientific Computing Center (NERSC) a U.S. Department of Energy Office of Science User Facility operated under Contract No. DE-AC02-05CH11231, and the Extreme Science and Engineering Discovery Environment (XSEDE) which is supported by National Science Foundation Grant No. ACI-1548562[43].

AUTHOR CONTRIBUTIONS

J.X. performed the first-principles calculations. J.X. and Y.P. analyzed the results. J.X. and Y.P. designed all aspects of the study. J.X. and Y.P. wrote the manuscript.

COMPETING INTERESTS

The authors declare no competing interests.

ADDITIONAL INFORMATION

Supplementary information The online version contains supplementary material available at https://doi.org/10.1038/s41524-023-00992-y.

Correspondence and requests for materials should be addressed to Junqing Xu or Yuan Ping.

Reprints and permission information is available at http://www.nature.com/reprints

Publisher's note Springer Nature remains neutral with regard to jurisdictional claims in published maps and institutional affiliations.